Widespread polar stratospheric ice clouds in the 2015/2016 Arctic winter – Implications for ice nucleation

Christiane Voigt[1,2], Andreas Dörnbrack[1], Martin Wirth[1], Silke M. Groß[1], Michael C. Pitts[3], Lamont R.

Poole[4], Robert Baumann[1], Benedikt Ehard[1], Björn-Martin Sinnhuber[5], Wolfgang Woiwode[5], Hermann

Oelhaf[5]

[1]Institute of Atmospheric Physics, Deutsches Zentrum für Luft- und Raumfahrt (DLR), Oberpfaffenhofen, 82234, Germany.
[2]Institute of Atmospheric Physics, Johannes Gutenberg-University, Mainz, 55881, Germany.
[3]NASA Langley Research Center, Hampton, VA, 23681, USA.
[4]Science Systems and Applications, Incorporated, Hampton, VA, 23681, USA.
[5]Institute of Meteorology and Climate Research, Karlsruhe Institute of Technology, Karlsruhe, 76131, Germany.

Correspondence to: Christiane Voigt (Christiane.Voigt@dlr.de)

Abstract. Low planetary wave activity led to a stable vortex with exceptionally cold temperatures in the 2015/2016 Arctic winter. Extended areas with temperatures below the ice frost point T_e persisted over weeks in the Arctic stratosphere as derived from the 36-year temperature climatology of the ERA-Interim reanalysis data set of the European Center for Medium Range Weather Forecast ECMWF. These extreme conditions promoted the formation of widespread polar stratospheric ice clouds (ice PSCs). The space-borne Cloud-Aerosol Lidar with Orthogonal Polarization CALIOP instrument onboard the onboard the CALIPSO satellite (Cloud-Aerosol Lidar and Infrared Pathfinder Satellite Observation) continuously measured ice PSCs for about a month with maximum extensions of up to 2×10^6 km^2 in the stratosphere. On 22 January 2016, the WALES (Water Vapor Lidar Experiment in Space - airborne demonstrator) lidar onboard the High Altitude and Long Range Research Aircraft HALO detected an ice PSC with a horizontal lengths of more than 1400 km. The ice PSC extended between 18 and 24 km altitude and was surrounded by nitric acid trihydrate (NAT) particles, supercooled ternary solution (STS) droplets and particle mixtures. The ice PSC occurrence in the backscatter ratio to depolarization optical space spanned by WALES observations is best matched by defining the inverse backscatter ratio of 0.3 as $1/R_{ice|NAT}$ threshold between ice and NAT cloud regions. In addition, the histogram clearly shows two distinct branches in ice PSC occurrence, indicative for two ice formation pathways. In addition to ice nucleation in STS$_m$ with meteoric dust inclusions, ice nucleation on pre-existing NAT may play a role in the Arctic winter 2015/2016. This hypothesis is tested using ECMWF trajectory analysis starting in the two ice branches. The observation of widespread Arctic ice PSCs can advance our

understanding of ice nucleation in cold polar and tropical latitudes. It further provides a new observational data base for the parameterization of nucleation schemes of ice PSCs in atmospheric models.

1 Introduction

While synoptic-scale ice PSCs commonly occur in the Antarctic winter stratosphere (Solomon et al., 1986), widespread ice
5   PSCs extending over several thousand km² have rarely been observed in the Arctic. Even since enhanced observational coverage of the polar regions by the CALIOP instrument (Pitts et al., 2009; Pitts et al., 2011) onboard the CALIPSO satellite, synoptic-scale ice PSCs were detected only occasionally in the Arctic (Pitts et al., 2013; Engel et al., 2013; Achtert and Tesche, 2014; Koshrawi et al., 2016). Generally Arctic stratospheric temperatures are above the ice frost point T_{ice} (Murphy and Koop, 2005) on synoptic scales and hence limit the formation of extended ice PSCs. The reason for the warmer
10   temperatures in the Arctic compared to the Antarctic is a more alternated land-ocean contrast in the northern hemisphere, supporting the generation of planetary waves, which disturb and hence weaken the Arctic polar vortex due to inmixing of warmer mid-latitude air (Solomon, 2004). In addition, radiative heating of the displaced and elongated vortex contributes to warmer Arctic vortex temperatures.

Ice PSCs exist at cold conditions with temperatures below T_{ice}, while other PSC types prevail at higher temperatures. These
15   can contain NAT particles (Voigt et al., 2000a; Fahey et al., 2001), STS (Dye et al., 1992; Carslaw et al., 1994; Schreiner et al., 1999a; Voigt et al., 2000b) and their mixtures. Complementary to in-situ particle composition measurements (e.g. Schreiner et al., 1999b, Northway et al., 2002), lidar measurements led to a cloud type classification based on the optical properties of solid or liquid PSC particles (Toon et al., 2000). PSCs with depolarization below 0.04 at 532 nm wavelength were classified as STS (Pitts et al., 2009). PSCs with higher depolarization were labelled Mix1 and Mix2, probably NAT
20   clouds with lower or higher NAT particle number densities, respectively, and some amounts of STS. Finally depolarizing PSCs with backscatter ratios above 5 were classified as ice. Later studies (Pitts et al., 2011; Pitts et al., 2013; Achtert and Tesche, 2014) led to an even more detailed differentiation of PSC types.

Large ice crystals in PSCs may sediment down and transport water vapor to lower altitudes (Fahey et al., 1990; Schiller et al., 2002). Further, due to their large surface areas, ice PSCs very efficiently process halogen compounds (Hanson and
25   Ravishankara, 1992) and hence contribute to ozone loss (Toon et al., 1989). Processing of halogenated reservoir gases on PSC particles leads to a release of unstable chlorine and bromine species, which become activated by sunlight in polar spring and effectively destroy ozone in catalytic cycles (Farman et al., 1985; Crutzen and Arnold, 1986). Ozone depletion is stopped, when the activated chlorine and bromine species react with nitrogen dioxide to reform stable reservoirs. The deactivation of chlorine species can be delayed under denitrified conditions, when the nitric acid concentration in the
30   stratosphere is reduced through sedimenting NAT particles or nitric acid containing ice particles. In the absence of ice at warmer temperatures, other PSC types can provide surfaces necessary for heterogeneous chlorine processing (Grooß et al., 2005; Manney et al., 2011; Drdla and Müller, 2012). E.g. in the Arctic winters 2009/10 and 2010/11 (Manney et al., 2011;

Sinnhuber et al., 2011; von Hobe et al., 2013), polar ozone loss was largely driven by STS aerosol (Wohltmann et al., 2013) and NAT (Nakajima et al., 2016). Using multi-year global modeling, Kirner et al. (2015) suggest that also in the Antarctic, a major fraction of ozone loss results from chlorine processing on liquid aerosol. In these cases, the role of ice as transporter for nitric acid enhancing denitrification and slowing down ozone loss may gain importance.

5 Ice PSCs may nucleate homogeneously in liquid STS aerosol or heterogeneously by the aid of solid particles (Toon et al., 1989; Peter, 1997; Zondlo et al., 2000). Homogeneous ice nucleation in STS may occur at high cooling rates as observed in localized mountain wave events (Dörnbrack et al., 2002). On synoptic scales, homogeneous ice nucleation rates (Koop et al., 2000) generally are too low to allow for homogeneous ice nucleation in the Arctic. Heterogeneous ice nucleation in STS with meteoric dust (Cziczo et al., 2001; Curtius et al., 2005; Weigel et al., 2014) aided by small scale temperature

10 fluctuations helped to explain the formation of a synoptic-scale ice PSC in the Arctic observed in January 2010 (Pitts et al., 2013; Engel et al., 2013).

Here we present new measurements of large scale ice PSCs in the Arctic winter 2015/2016 and discuss ice nucleation pathways. In addition to ice nucleation in STS with meteoric dust inclusions as proposed by Engel et al. (2013), we suggest that ice nucleation on pre-existing NAT might be required to explain a second branch in the ice PSC occurrence histogram.

15 First, we describe the instrumentation and methods. Then we give an overview of the meteorological condition, which led to a strong cooling of the polar vortex in the Arctic winter 2015/2016. Ice PSCs were observed over elongated periods by the spaceborne CALIOP lidar as described in section 4. On 22 January 2016, differential absorption lidar measurements of an elongated ice PSC were performed onboard the HALO research aircraft during the POLSTRACC (Polar Stratosphere in a Changing Climate) campaign. Based on the PSC occurrence histogram in the backscatter ratio to depolarization optical

20 space, we define a threshold for the $1/R_{ice|NAT}$ threshold for ice and investigate the effect of different thresholds on ice PSC occurrence in sensitivity studies. The PSC histogram shows two branches in ice PSC occurrence. We calculate back-trajectories starting in each of the two branches and investigate possible ice formation pathways for each branch. Finally we discuss the implications of the suggested ice formation pathway on NAT for Arctic PSCs and tropical ice clouds and suggest a way forward for PSC modeling.

2 Instrumentation and methods

In this study, we use lidar measurements from the research aircraft HALO and from the CALIPSO spacecraft in combination with meteorological data from the European Centre for Medium-Range Weather Forecasts (ECMWF) numerical weather prediction model to investigate occurrence and formation of ice PSCs in the Arctic winter 2015/2016 with a special focus on 22 January 2016.

30

2.1 WALES lidar measurements on HALO during the POLSTRACC campaign

From 7 December 2015 till 20 March 2016, the international field campaign PGS (POLSTRACC/GW-CYCLE/SALSA) was conducted with the High Altitude and Long Range Gulfstream G550 research aircraft HALO out of Oberpfaffenhofen, Germany (48°N, 11°E) and Kiruna, Sweden (68°N, 20°E). The POLSTRACC campaign particularly focused on investigating polar stratospheric chemistry and dynamics in the 2015/2016 Arctic winter. With a ceiling altitude of 15 km HALO is perfectly suited to study the evolution of the lower part of the polar vortex and to provide specific in-situ PSC information at these altitudes.

PSC abundance above HALO flight altitudes was detected with the WALES lidar instrument (Wirth et al., 2010; Groß et al., 2014). The WALES lidar as configured during POLSTRACC has backscatter channels at 532 nm and 1064 nm wavelengths and additionally a high spectral resolution lidar (HSRL) channel and a depolarization channel at 532 nm wavelength for particle detection. The HSRL capability allows the retrieval of the extinction corrected backscatter coefficient of clouds at 532 nm without assumptions about the phase function of the particles (Esselborn, 2008). The backscatter ratio R is the ratio of the un-attenuated (extinction corrected) total (unpolarized) backscatter coefficient and the molecular backscatter. The extinction correction is done by the HSRL channel using a molecular reference profile calculated from pressure and temperature data from ECMWF operational analyses at ~ 16 km horizontal resolution (6 h temporal resolution) and short term forecasts (1 h steps) to interpolate between the analyses. Linear particle depolarization is derived from volume polarization data and backscatter ratio, following the method outlined by Freudenthaler et al. (2009). The relative sensitivity of the two polarized channels is recalibrated regularly during flight to guarantee reliable depolarization values.

2.2 Spaceborne CALIOP lidar data

The Cloud-Aerosol Lidar with Orthogonal Polarization (CALIOP) lidar on board the Cloud-Aerosol Lidar and Infrared Pathfinder Satellite Observations (CALIPSO) satellite measures backscatter at wavelengths of 1064 nm and 532 nm, with the 532 nm signal separated into parallel and perpendicular polarization components. The general performance of CALIOP and calibration of the CALIOP data are discussed in Hunt et al. (2009) and Powell et al. (2009). The PSC results in this paper are based on the Version 2.0 CALIOP PSC detection and composition discrimination algorithm (Poole and Pitts, 2017), which uses nighttime-only profiles from 8.2 to 30 km altitude of CALIOP V4.10 Lidar Level 1B 532 nm data smoothed to a uniform 5 km horizontal (along track) by 180 m vertical resolution grid.

Following the methodology of Pitts et al. (2009; 2013), PSCs are detected as statistical outliers relative to the background stratospheric aerosol population in either 532 nm perpendicular backscatter (β_{perp}) or 532 nm scattering ratio R, which is the ratio of total backscatter to molecular backscatter. Successive horizontal averaging (5, 15, 45, and 135 km) is also used to ensure that strongly scattering PSCs (e.g., fully developed STS and ice) are found at the finest possible spatial resolution while also enabling the detection of more tenuous PSCs (e.g., low number density liquid-NAT mixtures) through additional averaging.

CALIOP PSC composition classification is based on comparing CALIOP data with temperature-dependent theoretical optical calculations of β_{perp} and R for non-equilibrium mixtures of liquid (binary H_2SO_4-H_2O or STS) droplets and NAT or ice particles. In regard to this paper, the main improvement in the Version 2.0 PSC algorithm is that the threshold value of R separating ice and NAT mixture PSCs ($R_{ice|NAT}$) is calculated as a function of altitude and time based on the observed abundance of nitric acid and water as estimated from nearly coincident Aura MLS measurements (Manney et al., 2016). Thus the Version 2.0 $R_{NAT|ice}$ (or $1/R_{NAT|ice}$) takes into account the impact of denitrification/dehydration on the optical signature of ice and NAT mixture clouds. In mid-late January 2016, $1/R_{NAT|ice}$ ranges between 0.2 and 0.4 in the 18-24 km altitude region.

The CALIPSO PSC areal coverage is estimated as the sum of the occurrence frequency (number of PSC detections divided by the total number of observations) in ten equal area latitude bands spanning 90°-50° N, multiplied by the area of each band. We assume that the CALIOP observations from the approximately 15 daily orbits are representative of the PSC coverage within each latitude band. The data are aggregated on daily time scales and smoothed over 7 days to reduce noise.

2.3 Meteorological data sets

We use meteorological data from two operational analyses of the Integrated Forecasting System (IFS) of the European Centre for Medium-Range Weather Forecasts (ECMWF) to describe the meteorological conditions of the polar stratosphere in winter 2015/2016. From December 2015 to March 2016, the IFS produced the operational analyses cycle 41r1 (T_L1279L137) with a horizontal resolution of about 16 km ($0.25° \times 0.25°$ at the equator) and the experimental IFS cycle 41r2 (T_C1279L137) simultaneously with a higher resolution of about 8 km ($0.125° \times 0.125°$ at the equator). The later IFS cycle became operational after 8 March 2016 (Holm et al., 2016). The enhanced horizontal resolution was achieved by changing from linear to cubic spectral truncation and introducing an octahedral reduced Gaussian grid (Malardel and Wedi 2016). Here, we show data in both resolutions for the 1 December 2015 to 8 March 2016 period to investigate the effects of a higher resolution on the meteorological data set, after 8 March 2016 the high resolution data are presented. We give 6-hourly operational analysis and use 1-hourly forecast data to interpolate between the time steps.

In addition, to compare to previous years, we use 6-hourly ERA-Interim reanalysis data (Dee et al. 2011) retrieved at a horizontal resolution of ($1° \times 1°$). ERA-Interim is a global atmospheric reanalysis from 1989 to today. The data assimilation system used to produce ERA-Interim data is based on the release of the IFS cycle 31r2 (T_L255L60) in 2006. The system includes a 4-dimensional variational analysis with a 6-hour analysis window. The spatial resolution of the data set is ~ 80 km horizontally on 60 vertical levels from the surface up to 0.1 hPa. ERA-Interim data can be downloaded from the ECMWF public datasets web interface or from MARS archive. A detailed documentation of the ERA-Interim data archive is given by Berrisford et al. (2011).

We derive the minimum temperature T_{min} (K) between 65° and 90°N at the 30-hPa pressure surface from the ERA-Interim reanalysis and from the two operational analyses of the IFS. We further calculate the area A_{ice} with temperatures below the ice frost point T_{ice} using Murphy and Koop (2005) and the area A_{NAT} with temperatures below the NAT equilibrium

temperature T_{NAT} using Hanson and Mauersberger (1988) for 4.6 ppmv H_2O and 7 ppbv HNO_3, as measured by MLS in the Arctic vortex in January 2016 (Manney and Lawrence, 2016).

3 Temperature evolution of the Arctic stratosphere in the 2015/2016 winter

The temperature evolution in the Arctic winter stratosphere is influenced by planetary wave activity. In early winter 2015 a strong tropical tropospheric temperature anomaly reinforced the meridional temperature gradient from the tropics to the poles which led to adverse conditions for the propagation of planetary waves (Matthias et al., 2016). Weak planetary wave activity measured as low meridional heat flux thus enforced the formation of a strong and stable polar vortex and caused extremely low temperatures in the Arctic winter 2015/2016 (Dörnbrack et al., 2016).

Therefore, stratospheric temperatures decreased dramatically as derived from the meteorological data of the IFS of the ECMWF numerical weather prediction model. Figure 1A shows the evolution of T_{min} at latitudes > 65°N and at 30 hPa in the Arctic winter 2015/2016 in two resolutions. In December 2015, T_{min} decreased below T_{ice} and then remained below T_{ice} from late December 2015 till end of January 2016. Within the first cold phase, T_{min} down to 182 K were detected in the operational IFS analysis with 16 km horizontal resolution. In February 2016, three minor stratospheric warmings influenced the vortex and led to warmer conditions in a coherent but slightly displaced polar vortex (Manney and Lawrence, 2016). Then, the final stratospheric warming resulted in a split of the vortex by mid-March and the subsequent dissipation of the vortices associated with a temperature increase of more than 20 K at 30 hPa in a few days.

The exceptional coldness of the Arctic winter 2015/2016 also reflects in the fact that by the end of December 2015, T_{min} dropped even below the minimum temperatures > 65°N at 30 hPa ever obtained by the ERA interim data record extending from 1989 to 2016 (Dee et al., 2011). Throughout the Arctic winter 2015/2016, T_{min} was continuously lower than the mean temperature of the 36-years ERA interim data record (Voigt et al., 2016), see Figure 1.

To illustrate the effect of mesoscale temperature fluctuations on T_{min}, we also show T_{min} derived from the IFS cycle 41r2 at ~ 8 km horizontal resolution compared to the cycle 41r1 at ~ 16 km resolution at 30hPa for the December 2015 to 8 March 2016 time period where both data sets are available. Temperature deviations up to 7 K between the higher and lower resolution data sets occurred during the first cold phase with $T_{min} < T_{ice}$ in December and early January as shown in Figure 1A. At higher resolution, minimum temperatures reach down to 179 K on the 30 hPa level. In the second cold period at the end of January 2016, temperature deviations up to 3 K are found in the higher resolution data set. Mesoscale gravity wave activity in December and January 2016 is better covered in the higher resolution data and could have caused this temperature difference (Dörnbrack et al., 2016). On 8 March 2016, the two data sets merge and from then on, ECMWF operational analysis are given at ~ 8 km resolution.

At 30 hPa, the area A_{ice} with $T < T_{ice}$ extended over regions up to 3.6×10^6 km^2 (see Figure 1B), as derived from IFS cycle 41r1 analysis at 16 km resolution. From 18 January till the end of the month, A_{ice} was continuously more than one order of magnitude larger than the 36-years average and larger than the maximum of the 36-years ERA interim data record. In

addition the area A_{NAT} with $T < T_{NAT}$ in January 2016 continuously reached the maximum of the 36-years ERA interim data set (Figure 1C). Generally A_{ice} and A_{NAT} are lower than the mean Antarctic conditions as given by the dashed gray line in Figure 1B and C (shifted by 6 months to account for seasonality).

These extremely cold stratospheric winter conditions in the Arctic set the stage for synoptic-scale PSC formation in winter 2015/2016.

4 Occurrence of ice PSCs in the Arctic winter 2015/2016 derived from CALIOP observations

The CALIOP lidar onboard the CALIPSO spacecraft detected PSCs from December 2015 to January 2016 (Figure 2). On 28 January 2016 the CALIOP science data acquisition was suspended due to a spacecraft anomaly. The problem was subsequently resolved and data acquisition began again on 14 March 2016.

Ice PSCs were measured by CALIOP continuously for a month from December 2015 to late January 2016 (Figure 2A). The ice PSCs were observed at altitudes between 15 and 25 km during the period with extremely cold temperatures inside the Arctic vortex. The maximum extension of ice PSCs derived from CALIOP $A_{ice,max}$ of $(1.75 – 2.0) \times 10^6$ km^2 is reached on 30 December 2015. In this phase, the ice PSC formation was triggered by mountain wave activity and spread out to synoptic scales, see Dörnbrack et al. (2016). Considering the uncertainties in A_{ice} retrieval from the CALIOP data set interpolated to latitude bands, the maximum $A_{ice,max}$ derived from CALIOP observations agrees reasonably with $A_{ice,max}$ derived from weather forecast IFS data of 2.1×10^6 km^2 at 30 hPa (~21.6 km). Also the second peak in ice PSC occurrence A_{ice} on 24 January 2016 is captured by the CALIOP routine though with a smaller peak amplitude. A decrease of water vapor concentrations and dehydration due to falling ice crystals has been observed by MLS (Manney and Lawrence, 2016) at these altitudes throughout January 2016. This may explain lower A_{ice} derived from CALIOP data at the end of January compared to A_{ice} derived from in the IFS data set using a fixed H_2O mixing ratio of 4.6 ppmv to calculate A_{ice}.

NAT and STS PSCs were present in the CALIOP data set from early December 2015 till the end of the observation period (Figure 2B). As soon as temperatures decrease below T_{ice} on 21 December 2015, ice PSCs are present in the CALIOP data set. The immediate onset of ice PSCs at $T < T_{ice}$ may point to heterogeneous ice nucleation, as discussed in more detail later. Summarized, we find strong evidence for the unprecedented existence of widespread ice PSCs in the Arctic winter 2015/2016.

5 Optical properties of the PSC measured on 22 January 2016

PSCs were detected with the WALES lidar inside the vortex on all 6 HALO flights between 22 January and 29 February 2016. Before that data, the lidar on HALO was not operational. Due to the strong temperature increase at the end of January and measurement locations of HALO in warmer parts of the vortex, extended ice PSCs were observed by WALES solely on 22 January 2016.

5.1 Extension of the PSC on 22 January 2016

A large synoptic scale PSC was measured by WALES during a flight from Kiruna to the northern tip of Greenland on 22 January 2016 as shown in Figure 3. The PSC extended between 14 and 25 km altitude over a horizontal distance of 2200 km. It was continuously observed within in the Arctic vortex from 72°N to the outermost return point at 86°N. High backscatter ratios are indicators for the presence of large particle surfaces and high depolarization ratios suggest the presence of solid particles. The co-located measurements of the particle backscatter ratio and depolarization ratio thus allow for a cloud classification into different PSC types.

5.2 Classification of the PSC measured on 22 January 2016

Figure 4 shows the joint occurrence histogram of the inverse backscatter ratio 1/R and particle depolarization for the PSC measurements in Figure 3. The histogram bin size is 0.02×0.02 and the color scale indicates the number of cloud observations (4 km horizontal by 100 m vertical) falling within each bin. Overlaid are the regions which correspond to different PSC types following Pitts et al. (2011) with two modifications. First the sub-classification of Mix2 into Mix2-enhanced and normal Mix2 is dropped. Second, the $1/R_{ice|NAT}$ threshold for ice and NAT regions is set to 0.3. Without the latter change, a substantial part of the branch connecting STS and fully developed ice clouds would have been counted as NAT/Mix2 instead of ice, while ice is the more obvious interpretation of the lower branch in the ice class given the form of the joint histogram.

Interestingly, we find two branches for ice in the joint histogram, the lower one connected to the STS class and the upper one connected to the NAT/Mix2 regime. The NAT/Mix2 regime with enhanced NAT particle concentrations is strongly populated. In contrast, no observation falls into the wave ice class forming in strong mountain waves.

We now use the classification by Pitts et al. (2011) and the threshold of $1/R$ $R_{ice|NAT} = 0.3$ of ice versus NAT/Mix2 to classify the PSC from Figure 3. A large ice PSC (red areas in Figure 5) extends in a cloud layer with a vertical thickness up to 6 km between 18 and 24 km altitude over distances of over 1400 km. The synoptic-scale ice PSC is observed mainly at temperatures below T_{ice}. In the northern part of the cloud between 12:20 and 14:00 UTC, the ice PSC is surrounded by NAT/Mix2 cloud layers (yellow area) extending above and near the ice PSC to the North. Within the ice PSC, NAT can be masked by the higher optical signal from ice, but may be present. The combination of a high depolarization ratio with a quite low color ratio (ratio of the backscatter coefficient for the 532 nm channel and the 1064 nm channel, not shown here) of 1.5 at the bottom of the PSC (green area) points to larger NAT particle sizes, thus suggesting sedimenting NAT particles in the lowest part of the cloud. In addition, the southernmost part of the PSC observed between 15:15 and 16:00 UTC (blue) consists of non-depolarizing liquid STS droplets. The STS layer extends towards the south and below the ice layer.

5.3 Sensitivity study of the effect of different $R_{ice|NAT}$ thresholds on PSC classification

As discussed previously, the $1/R_{ice|NAT}$ threshold of 0.3 best matches the ice PSC observations in the lower branch of the PSC occurrence histogram in Figure 4. Nevertheless, we explore the effect of different $1/R_{ice|NAT}$ thresholds (0.3, 0.2, and a variable threshold var $= 0.20 < 1/R_{ice|NAT} < 0.31$) on ice PSC occurrence in Figure 6. In addition to the PSC classification for different thresholds, we add the region with temperatures below T_{ice} based on meteorological temperature data from the integrated forecast system IFS (cycle 41r1) of ECMWF and measured water vapor mixing ratios. For the $1/R_{ice|NAT}$ threshold of 0.3 the PSC area classified as ice by WALES $A_{ice,WALES}$ agrees best with A_{ice} derived from weather predictions. This is evident in particular between 22 and 24 km.

For comparison, we show results from the classification with the variable threshold $1/R_{ice|NAT} = $ var used in the CALIOP climatology in Figure 2. The $1/R_{ice|NAT} = $ var threshold is described in more detail in section 2.2 and uses a dynamic, altitude dependent variation of the $1/R_{ice|NAT}$ boundary between $0.20 < 1/R_{ice|NAT} < 0.31$ based on observed abundances of HNO_3 and H_2O. For this case, $A_{ice,WALES}$ is slightly lower than A_{ice} from meteorological analysis in particular between 22 and 24 km. Further, the $1/R_{ice|NAT} = 0.2$ threshold leads to even lower $A_{ice,WALES}$. For our case, the relative difference of $A_{ice,WALES}$ for $1/R_{ice|NAT} = $ var compared to $1/R_{ice|NAT} = 0.3$ is 8.2%. The relative difference relative of $A_{ice,WALES}$ for $1/R_{ice|NAT} = 0.2$ to $1/R_{ice|NAT} = 0.3$ amounts to 21.8%.

As also derived from the histogram plot in Figure 4, the $1/R_{ice|NAT} = 0.3$ threshold best matches the ice PSC observations by WALES at temperatures below T_{ice} on 22 January 2016. However, the $1/R_{ice|NAT} = $ var threshold might be an appropriate fit for the CALIOP data evaluation with changing HNO_3 and H_2O concentrations throughout the winter 2015/2016.

6 Discussion of ice PSC formation

We now discuss PSC formation in two steps based on the WALES lidar observations combined with trajectory analysis. First we investigate the formation of the ice, NAT and STS layers of the PSC observed on 22 January 2016 using 10 days back-trajectories starting in the different PSC layers with the starting points shown in Figure 5. Then we differentiate the ice PSC layer into two ice branches as derived from the backscatter ratio to depolarization occurrence histogram in Figure 4 and discuss ice formation pathways for the two ice regimes detected on 22 January 2016: the upper ice branch connecting ice to the NAT/Mix2 regime and the lower ice branch connecting ice to the STS regime. We start with the discussion of the formation of the ice, NAT and STS layers based on trajectory analysis.

6.1 Temperature history of trajectories starting in ice, NAT or STS PSC layers

The trajectory calculations were performed using the Hybrid Single-Particle Lagrangian Integrated Trajectory dispersion model HYSPLIT (Draxler, 1998) with operational forecast of the deterministic IFS (cycle 41r1 interpolated to $0.25 \times 0.25°$) from ECMWF at 3-hourly time steps as meteorological input. The HALO flight track and ECMWF temperatures at 30 hPa on 22 January 2016 are shown in Figure 7. We calculated backward-trajectories starting in the PSC observations every 2 min

at 30 hPa (about 21.6 km altitude) to investigate PSC formation. Further we performed sensitivity studies every 2 minutes at higher and lower altitudes (19, 21 and 23 km) to account for particle sedimentation, which is not included in the simplified trajectory calculations shown here. As a rough estimate, a 10-µm sized ice crystal sediments about 1 km in a day (Fahey et al., 2001). For aspherical particles the sedimentation rates are even lower (Woiwode et al., 2014; Woiwode et al., 2016;

5 Weigel et al., 2014;), hence generally our simplified calculations cover the altitude range of sedimenting PSC particles.

For reasons of clarity, in Figure 7 we show typical backward-trajectories starting in the ice PSC at 30 hPa at the location corresponding to WALES measurements (Figure 5) taken at 11:20, 11:35, 11:50 and 12:15 UTC (labels 1-4), in the NAT layer at 12:40 (label 5), and in the STS layer at 15:45 (label 6). The starting points in the ice PSC are marked by diamonds, NAT is symbolized by a square and STS by a circle.

10 For the ice layers, the trajectories' temperatures decrease below T_{ice} ~12 h prior to the observations during a slow uplift over Greenland. In contrast, the typical NAT trajectory 5 circulates within the inner vortex at temperatures below 188 K for 10 days without passing over Greenland. Therefore temperatures stay above T_{ice} throughout that period, excluding ice formation. Furthermore, the typical STS trajectory 6 experiences higher temperatures as it is located towards he edge of the polar vortex, and only drops below T_{NAT} one day before the PSC observation. Further it never decreases below $T_{ice}+2K$.

15 Thus, the trajectories starting in the different PSC layers within a single synoptic-scale PSC show different temperature histories which explain the formation of different particle types: ice, NAT or STS.

6.2 Nucleation pathways of the two ice branches

The existence of the two branches in the ice regime linked directly to STS or NAT/mix2 regimes respectively as shown in Figure 4 suggests two different ice nucleation pathways. (1) Ice nucleation in STS with potential inclusion of meteoric

20 material as suggested by Engel et al. (2013) may account for the lower STS-ice branch. Small meteoric inclusions in STS are below the detection limit of the WALES lidar but may be present. (2) A second ice nucleation pathway is required to explain the formation of the upper ice branch. The direct connection to the NAT regime points to ice nucleation on pre-existing NAT particles. The hypothesis of two different ice nucleation pathways for the 22 January 2016 ice PSC is investigated in more detail using trajectories starting the two specific ice PSC branches. Thereby the location of the NAT-ice branch within the

25 PSC curtain plot (Figure 5) is marked by the red area enclosed by the black line. We mark trajectory 4 starting in the upper ice branch connected the NAT regime by the white diamond in Figures 5 and 7. Further, trajectories 1 to 3 are related to the lower ice branch linked to the STS regime and are marked by gray diamonds in Figures 5 and 7.

Trajectory 4 (NAT-ice) decreases below T_{NAT} 7 days prior to the observations and remains below T_{NAT} till the observation. One day prior to the observations the trajectory reaches the Northern tip of Greenland and is slowly lifted and cools down.

30 hours later the temperatures decrease below T_{ice} allowing for ice nucleation on NAT. Hence, NAT particles had time to grow for ~ 7 days and then ice can heterogeneously nucleate on NAT at $T<T_{ice}$. NAT nucleation rates on meteoric dust (Voigt et al., 2005; Grooß et al., 2005; Hoyle et al., 2013) explain the formation of NAT PSCs within few days. Consistently, CALIOP observations indicate the presence of NAT clouds throughout January 2016.

In contrast, the temperatures of trajectories 1 to 3 starting in the STS-ice branch are higher and decrease below T_{NAT} one day prior to the observation. During that time, the trajectories are slowly lifted above central Greenland by ~1 km till temperatures below T_{ice} are reached at the lee-ward edge of Greenland. Timescales for NAT nucleation are small and cannot explain NAT/mix2 particle compositions. Ascent rates of 1 km/day are significantly lower than observed in strong mountain

5   wave events (Dörnbrack et al., 2002; Füglisthaler et al., 2002; Luo et al., 2003) and the wave ice class is absent in the PSC. However, we cannot exclude that moderate gravity wave activity might have induced temperature fluctuations when the trajectories pass perpendicular to the coast of Greenland. The trajectories and ice PSC occurrence point to heterogeneous ice nucleation in STS with meteoric inclusion as suggested by Engel et al. (2013) for the synoptic scale ice PSC observed in winter 2010. The influence of the orography decreases towards the northern tip of Greenland and when trajectories pass

10   aside of Greenland.

Sensitivity analysis has been performed for trajectories starting every 2 min in the PSC observed during the inbound flight leg to Kiruna at 30 hPa (not shown here for reasons of clarity). The trajectories for the inbound flight leg show a similar behavior, consistent with the analysis of the outbound flight leg towards the Northern tip of Greenland. Similar analysis holds for trajectories calculated at 21 and 23 km altitude. Summarized, the trajectory analysis supports our hypotheses of ice

15   nucleation in STS with meteoric inclusions for the ice PSC located in the lower branch of the PSC occurrence histogram. Here the trajectories are initially warm and temperatures decrease to $T < T_{ice}$ when trajectories pass over Greenland 12 hours prior to the measurements. A second nucleation pathway could be ice nucleation on NAT for the upper ice branch in the PSC occurrence histogram. Here, the trajectories are below T_{NAT} for 7 days and then pass over the Northern tip of Greenland where a slight lift leads to temperatures below T_{ice}. Further north, as indicated by NAT trajectory 5, the trajectories miss Greenland

20   and do not cool down, hence NAT remains. Thus the NAT-ice branch is connected to the NAT cloud located towards the norths in the center of the vortex.

7 Conclusions and outlook

Extremely low temperatures existed in the Arctic stratospheric winter 2015/2016 because low planetary wave activity resulted in a stable vortex. Synoptic-scale ice PSCs formed in late December 2015 and persisted throughout January as

25   observed by the CALIOP lidar onboard the CALIPSO satellite. The sedimentation of the ice PSC particles led to significant dehydration (Koshrawi et al., 2017). From January to early March 2016, water vapor data MLS data show severe dehydration between 400 and 500 K potential temperatures (Manney and Lawrence, 2016). In addition, ice PSCs can serve as efficient transporters for nitric acid incorporated into ice. Large ice particles sediment faster than smaller NAT particles and therefore ice can lead to efficient denitrification at PSC altitudes. Massive denitrification has been measured by MLS

30   with an onset in mid-December 2015 throughout the Arctic winter (Manney and Lawrence, 2016; Khosrawi et al., 2017). We use high resolution WALES lidar measurements of a large-scale ice PSC observed on 22 January 2016 to investigate ice nucleation pathways. Two distinct branches in the ice PSC occurrence histogram suggest two ice formation pathways: ice

nucleation in STS with meteoric inclusions as suggested by Engel et al. (2013) and, in addition, ice formation on NAT. While the lower STS-ice branch is frequently populated in space-borne CALIOP lidar data, the upper NAT/Mix2-ice branch is rarely observed by CALIOP in Arctic or Antarctic PSC measurements (Pitts et al., 2013). Larger noise in the satellite data with CALIPSO travelling at an orbit near 700 km and a higher detection limit of the CALIOP lidar data compared to the

5   WALES measurements on aircraft cruising at 14 km altitude explains this difference. Thus the global abundance of ice PSCs nucleated on NAT cannot be assessed with the present lidar data set. Global high resolution lidar observations are required to estimate the global occurrence of the upper ice branch and of NAT/Mix2 layers. These observations could then help to evaluate the importance of the suggested NAT-ice nucleation pathway in other regions of the atmosphere. Further, additional lidar or in-situ observations from aircraft (Fahey et al., 2001; Northway et al., 2002) could help to answer the question on the

10   abundance of the upper NAT branch, which might include aspherical NAT particles as observed by Molleker et al. (2014) and Woiwode et al. (2016). Generally this branch is of importance for denitrification.

The NAT crystal has a stoichiometry of 1 $HNO_3 \times 3$ H_2O molecules and exists in α–NAT or β–NAT crystal structure (Iannarelli and Rossi, 2015). Compared to liquid aerosol or meteoric particles, the NAT crystal structure is more similar to that of ice, and therefore NAT readily nucleates on ice as frequently observed in laboratory experiments (Hanson and

15   Mauersberger, 1988; Iannarelli and Rossi, 2015; Gao et al., 2016; Weiss et al., 2016) and in mountain wave ice PSCs (Carslaw et al., 2002; Fueglistaler et al., 2002; Luo et al., 2003; Voigt et al., 2003). Vice versa, we propose here that ice may nucleate on NAT. Direct laboratory measurements of the nucleation rate of ice on NAT are missing (Koop et al., 1997) and would be required to provide further evidence of the suggested ice nucleation process.

Ice nucleation on NAT may be responsible for the early onset of ice PSC formation in December 2015. CALIOP data show

20   that ice PSCs were observed as soon as temperatures decreased below T_{ice}. Further, ice nucleation on NAT may occur in the tropical tropopause, where the existence of a NAT belt and cirrus has been detected (Popp et al., 2007, Voigt et al., 2008). Based on the observational data set, the ice nucleation rate on NAT could be parameterized and implemented in a large scale model in order to assess the global relevance the different ice PSC nucleation pathways in different regions of the atmosphere.

Data availability: The observational data are available at https://halo-db.pa.op.dlr.de. Operational meteorological analysis are achieved in the MARS archive at ECMWF (https://www.ecmwf.int/en/forecasts/documentation-and-support/changes-ecmwf-model/ifs-documentation), ERA-Interim data were taken from https://www.ecmwf.int/en/research/climate-reanalysis/era-interim.

30

Author contributions: CV performed the scientific study and wrote the paper. AD and BE analyzed the meteorological conditions for the Arctic winter 2016. MW and SG performed the HALO lidar measurements and data evaluation. MP and LP evaluated CALIPSO data. RB made the HYSPLIT trajectory calculations. BMS, WW and HO were the coordinators of

the POLSTRACC campaign. All authors contributed to the manuscript. The authors declare that they have no conflict of interest.

Acknowledgements: We thank the DLR flight department for excellent support of the campaign. Further we thank H. Ziereis, T. Jurkat, S. Kaufmann for helpful comments on the manuscript. Support for the campaign was provided by the HALO-SPP 1294 program and the Helmholtz society via the ATMO program. CV has been funded by the Helmholtz society under contact no W2/W3-060 and by DFG contract no VO1504/4-1, BE by DFG contract no DO1400/6-1. Support for MP and LP is provided by the NASA CALIPSO/CloudSat Science Team.

References

Achtert, P., and M. Tesche: Assessing lidar-based classification schemes for polar stratospheric clouds based on 16 years of measurements at Esrange, Sweden, J Geophys Res-Atmos, 119, 1386–1405, doi:10.1002/2013JD020355, 2014.

Berrisford, P., Dee, D., Poli, P., Brugge, R., Fielding, K., Fuentes, M., Kallberg, P., Kobayashi, S., Uppala, S., Simmons, A. The ERA-Interim archive Version 2.0, ERA Report Series 1, ECMWF, Shinfield Park, Reading, UK, 2011.

Bohlinger, P., Sinnhuber, B. M., Ruhnke, R., and Kirner, O.: Radiative and dynamical contributions to past and future Arctic stratospheric temperature trends, Atmos. Chem. Phys., 14, 1679-1688, doi:10.5194/acp-14-1679-2014, 2014.

Carslaw, K.S., Luo, B.P., Clegg, S.L., Peter, Th., Brimblecombe, P., Crutzen, P.J.: Stratospheric aerosol growth and HNO_3 and water uptake by liquid particles, Geophys Res Lett, 21, 2479–2482, 1994.

Carslaw, K. S., Kettleborough, J. A., Northway, M. J., Davies, S., Gao, R. S., Fahey, D. W., Baumgardner, D. G., Chipperfield, M. P., and Kleinbohl, A.: A vortex-scale simulation of the growth and sedimentation of large nitric acid hydrate particles, J Geophys Res-Atmos, 107, doi:10.1029/2001jd000467, 2002.

Crutzen, P. J., and Arnold, F.: Nitric-Acid Cloud Formation in the Cold Antarctic Stratosphere - a Major Cause for the Springtime Ozone Hole, Nature, 324, 651-655, doi:10.1038/324651a0, 1986.

Curtius, J., Weigel, R., Vössing, H.-J., Wernli, H., Werner, A., Volk, C.-M., Konopka, P., Krebsbach, M., Schiller, C., Roiger, A., Schlager, H., Dreiling, V., and Borrmann, S.: Observations of meteoric material and implications for aerosol nucleation in the winter Arctic lower stratosphere derived from in situ particle measurements, Atmos. Chem. Phys., 5, 3053-3069, https://doi.org/10.5194/acp-5-3053-2005, 2005.

Cziczo, D. J., Thomson, D. S., and Murphy, D. M.: Ablation, flux, and atmospheric implications of meteors inferred from stratospheric aerosol, Science, 291, 1772-1775, doi:10.1126/science.1057737, 2001.

Dee, D. P., Uppala, S. M., Simmons, A. J., Berrisford, P., Poli, P., Kobayashi, S., Andrae, U., Balmaseda, M. A., Balsamo, G., Bauer, P., Bechtold, P., Beljaars, A. C. M., van de Berg, L., Bidlot, J., Bormann, N., Delsol, C., Dragani, R., Fuentes, M., Geer, A. J., Haimberger, L., Healy, S. B., Hersbach, H., Holm, E. V., Isaksen, L., Kallberg, P., Kohler, M., Matricardi, M., McNally, A. P., Monge-Sanz, B. M., Morcrette, J. J., Park, B. K., Peubey, C., de Rosnay, P., Tavolato, C., Thepaut, J. N., and Vitart, F.: The ERA-Interim reanalysis: configuration and performance of the data assimilation system, Quat. Journ. Roy. Meteor. Soc., 137, 553-597, 10.1002/qj.828, 2011.

Dörnbrack, A., Birner, T., Fix, A., Flentje, H., Meister, A., Schmid, H., Browell, E. V., and Mahoney, M. J.: Evidence for inertia gravity waves forming polar stratospheric clouds over Scandinavia, J Geophys Res-Atmos, 107, doi:10.1029/2001jd000452, 2002.

Dörnbrack, A., Gisinger, S., Pitts, M. C., Poole, L. R., and Maturilli, M.: Multilevel cloud structures over Svalbard, Monthly Weather Review, doi:10.1175/mwr-d-16-0214.1, 2016.

Draxler, R. R., and G. D. Hess: An overview of the HYSPLIT4 modeling system of trajectories, dispersion, and deposition, Aust. Meteor. Mag., 47, 295–308, 1998.

Drdla, K., and Müller, R.: Temperature thresholds for chlorine activation and ozone loss in the polar stratosphere, Ann. Geophys., 30, 1055-1073, doi:10.5194/angeo-30-1055-2012, 2012.

Dye, J. E., Baumgardner, D., Gandrud, B. W., Kawa, S. R., Kelly, K. K., Loewenstein, M., Ferry, G. V., Chan, K. R., and Gary, B. L.: Particle-Size Distributions in Arctic Polar Stratospheric Clouds, Growth and Freezing of Sulfuric-Acid Droplets, and Implications for Cloud Formation, J Geophys Res-Atmos, 97, 8015-8034, doi: 10.1029/91JD02740, 1992.

Engel, I., Luo, B. P., Pitts, M. C., Poole, L. R., Hoyle, C. R., Grooss, J. U., Dornbrack, A., and Peter, T.: Heterogeneous formation of polar stratospheric clouds - Part 2: Nucleation of ice on synoptic scales, Atmos. Chem. Phys., 13, 10769-10785, doi:10.5194/acp-13-10769-2013, 2013.

Esselborn, M., M. Wirth, A. Fix, M. Tesche, and G. Ehret: Airborne high spectral resolution lidar for measuring aerosol extinction and backscatter coefficients, Applied Optics, 47, 346-358, doi:10.1364/AO.47.000346, 2008.

Fahey, D. W., Kelly, K. K., Kawa, S. R., Tuck, A. F., Loewenstein, M., Chan, K. R., Heidt, L. E.: Observations of denitrification and dehydration in the winter polar stratospheres, Nature, 344, 321-324, doi:10.1038/344321a0, 1990.

Fahey, D. W., Gao, R. S., Carslaw, K. S., Kettleborough, J., Popp, P. J., Northway, M. J., Holecek, J. C., Ciciora, S. C., McLaughlin, R. J., Thompson, T. L., Winkler, R. H., Baumgardner, D. G., Gandrud, B., Wennberg, P. O., Dhaniyala, S., McKinney, K., Peter, T., Salawitch, R. J., Bui, T. P., Elkins, J. W., Webster, C. R., Atlas, E. L., Jost, H., Wilson, J. C., Herman, R. L., Kleinbohl, A., and von Konig, M.: The detection of large HNO3-containing particles in the winter arctic stratosphere, Science, 291, 1026-1031, doi:10.1126/science.1057265, 2001.

Farman, J. C., Gardiner, B. G., and Shanklin, J. D.: Large losses of total ozone in Antarctica reveal seasonal ClO_x/NO_x interaction, Nature, 315, 207–210, doi:10.1038/315207a0, 1985.

Freudenthaler, V., Esselborn, M., Wiegner, M., Heese, B., Tesche, M., Ansmann, A., Müller, D., Althausen, D., Wirth, M., Fix, A., Ehret, G., Knippertz, P., Toledano, C., Gasteiger, J., Garhammer, M. and Seefeldner, M.: Depolarization ratio profiling at several wavelengths in pure Saharan dust during SAMUM 2006. Tellus B, 61: 165–179. doi:10.1111/j.1600-0889.2008.00396.x, 2009.

Fueglistaler, S., Luo, B. P., Buss, S., Wernli, H., Voigt, C., Muller, M., Neuber, R., Hostetler, C. A., Poole, L. R., Flentje, H., Fahey, D. W., Northway, M. J., and Peter, T.: Large NAT particle formation by mother clouds: Analysis of SOLVE/THESEO-2000 observations, Geophys. Res. Lett., 29, doi:10.1029/2001gl014548, 2002.

Fueglistaler, S., Luo, B. P., Voigt, C., Carslaw, K. S., and Peter, Th.: NAT-rock formation by mother clouds: a microphysical model study, Atmos. Chem. Phys., 2, 93-98, https://doi.org/10.5194/acp-2-93-2002, 2002.

Gao, R. S., Gierczak, T., Thornberry, T. D., Rollins, A. W., Burkholder, J. B., Telg, H., Voigt, C., Peter, T., and Fahey, D. W.: Persistent Water-Nitric Acid Condensate with Saturation Water Vapor Pressure Greater than That of Hexagonal Ice, J. Phys. Chem. A, 120, 1431-1440, doi:10.1021/acs.jpca.5b06357, 2016.

Grooß, J.-U., Günther, G., Müller, R., Konopka, P., Bausch, S., Schlager, H., Voigt, C., Volk, C. M., and Toon, G. C.: Simulation of denitrification and ozone loss for the Arctic winter 2002/2003, Atmos. Chem. Phys., 5, 1437-1448, https://doi.org/10.5194/acp-5-1437-2005, 2005.

Groß, S., Wirth, M., Schäfler, A., Fix, A., Kaufmann, S., and Voigt, C.: Potential of airborne lidar measurements for cirrus cloud studies, Atmos. Meas. Tech., 7, 2745-2755, doi:10.5194/amt-7-2745-2014, 2014.

Hanson, D., and Mauersberger, K.: Laboratory Studies of the Nitric-Acid Trihydrate - Implications for the South Polar Stratosphere, Geophys. Res. Lett., 15, 855-858, doi:10.1029/Gl015i008p00855, 1988.

5   Hanson, D. R., and Ravishankara, A. R.: Investigation of the Reactive and Nonreactive Processes Involving ClONO2 and HCl on Water and Nitric Acid Doped Ice, J. Phys. Chem., 96, 2682-2691, doi:10.1021/J100185a052, 1992.

Hoyle, C. R., Engel, I., Luo, B. P., Pitts, M. C., Poole, L. R., Grooss, J. U., and Peter, T.: Heterogeneous formation of polar stratospheric clouds - Part 1: Nucleation of nitric acid trihydrate (NAT), Atmos. Chem. Phys., 13, 9577-9595, doi:10.5194/acp-13-9577-2013, 2013.

10   Hólm, E., R. Forbes, S. Lang, L. Magnusson, and S. Malardel: New model cycle brings higher resolution, ECMWF Newsletter, No. 147, ECMWF, Reading, United Kingdom, 14-19, 2016. (online at http://www.ecmwf.int/sites/default/files/elibrary/2016/16299-newsletter-no147-spring-2016.pdf)

Hunt, W. H., D. M. Winker, M. A. Vaughan, K. A. Powell, P. L. Lucker, and C. Weimer, 2009: CALIPSO lidar description and performance assessment. J. Atmos. Oceanic Technol., 26, 1214–1228, doi.org/10.1175/2009JTECHA1223.1, 2009.

15   Iannarelli, R., and Rossi, M. J.: The mid-IR Absorption Cross Sections of alpha- and beta-NAT (HNO3 * 3H2O) in the range 170 to 185K and of metastable NAD (HNO3 * 2H2O) in the range 172 to 182K, J Geophys Res-Atmos, 120, doi:10.1002/2015JD023903, 2015.

Kawa, S. R., Stolarski, R. S., Newman, P. A., Douglass, A. R., Rex, M., Hofmann, D. J., Santee, M. L., and Frieler, K.: Sensitivity of polar stratospheric ozone loss to uncertainties in chemical reaction kinetics, Atmos. Chem. Phys., 9, 8651-
20   8660, doi:10.5194/acp-9-8651-2009, 2009.

Kirner, O., Müller, R., Ruhnke, R., and Fischer, H.: Contribution of liquid, NAT and ice particles to chlorine activation and ozone depletion in Antarctic winter and spring, Atmos. Chem. Phys., 15, 2019-2030, https://doi.org/10.5194/acp-15-2019-2015, 2015.

Koop, T., Carslaw, K. S., and Peter, T.: Thermodynamic stability and phase transitions of PSC particles, Geophys. Res. Lett.,
25   24, 2199-2202, doi:10.1029/97gl02148, 1997.

Koop, T., Luo, B., Tsias, A., and Peter, T.: Water activity as the determinant for homogeneous ice nucleation in aqueous sloutions, Nature, 406, 611–614, doi:10.1038/35020537, 2000.

Khosrawi, F., Urban, J., Pitts, M. C., Voelger, P., Achtert, P., Kaphlanov, M., Santee, M. L., Manney, G. L., Murtagh, D., and Fricke, K.-H.: Denitrification and polar stratospheric cloud formation during the Arctic winter 2009/2010, Atmos.
30   Chem. Phys., 11, 8471-8487, https://doi.org/10.5194/acp-11-8471-2011, 2011.

Khosrawi, F., Kirner, O., Sinnhuber, B.-M., Johansson, S., Höpfner, M., Santee, M. L., Froidevaux, L., Ungermann, J., Ruhnke, R., Woiwode, W., Oelhaf, H., and Braesicke, P.: Denitrification, dehydration and ozone loss during the 2015/2016 Arctic winter 2015/2016, Atmos. Chem. Phys., 17, 12893-12910 https://doi.org/10.5194/acp-17-12893-2017, 2017.

Luo, B. P., Voigt, C., Fueglistaler, S., and Peter, T.: Extreme NAT supersaturations in mountain wave ice PSCs: A clue to NAT formation, J. Geophys. Res. Atmos., 108, 4441, doi:10.1029/2002jd003104, 2003.

Manney, G. L., Santee, M. L., Rex, M., Livesey, N. J., Pitts, M. C., Veefkind, P., Nash, E. R., Wohltmann, I., Lehmann, R., Froidevaux, L., Poole, L. R., Schoeberl, M. R., Haffner, D. P., Davies, J., Dorokhov, V., Gernandt, H., Johnson, B., Kivi, R., Kyro, E., Larsen, N., Levelt, P. F., Makshtas, A., McElroy, C. T., Nakajima, H., Parrondo, M. C., Tarasick, D. W., von der Gathen, P., Walker, K. A., and Zinoviev, N. S.: Unprecedented Arctic ozone loss in 2011, Nature, 478, 465-469, doi:10.1038/nature10556, 2011.

Manney, G., and Lawrence, Z. D.: The major stratospheric final warming in 2016: Dispersal of vortex air and termination of Arctic chemical ozone loss, Atmos. Chem. Phys., 15371-15396, doi:10.5194/acp-16-15371-2016, 2016.

Malardel, S., and N. P. Wedi: How does subgrid-scale parametrization influence nonlinear spectral energy fluxes in global NWP models? J. Geophys. Res. Atmos., 121, 5395–5410, doi:10.1002/2015JD023970, 2016.

Matthias, V., A. Dörnbrack, and G. Stober: The extraordinary strong and cold polar vortex in the early northern winter 2015/2016, Geophys. Res. Lett., doi:10.1002/2016GL071676, 2016.

Molleker, S., Borrmann, S., Schlager, H., Luo, B., Frey, W., Klingebiel, M., Weigel, R., Ebert, M., Mitev, V., Matthey, R., Woiwode, W., Oelhaf, H., Dörnbrack, A., Stratmann, G., Grooß, J.-U., Günther, G., Vogel, B., Müller, R., Krämer, M., Meyer, J., and Cairo, F.: Microphysical properties of synoptic-scale polar stratospheric clouds: in situ measurements of unexpectedly large HNO_3-containing particles in the Arctic vortex, Atmos. Chem. Phys., 14, 10785-10801, https://doi.org/10.5194/acp-14-10785-2014, 2014.

Murphy, D. M., and Koop, T.: Review of the vapour pressures of ice and supercooled water for atmospheric applications, Q. J. R. Meteorol. Soc., 131, 1539–1565, doi:10.1256/qj.04.94, 2005.

Nakajima, H., Wohltmann, I., Wegner, T., Takeda, M., Pitts, M. C., Poole, L. R., Lehmann, R., Santee, M. L., and Rex, M.: Polar stratospheric cloud evolution and chlorine activation measured by CALIPSO and MLS, and modeled by ATLAS, Atmos. Chem. Phys., 16, 3311-3325, https://doi.org/10.5194/acp-16-3311-2016, 2016.

Northway, M. J., Gao, R. S., Popp, P. J., Holecek, J. C., Fahey, D. W., Carslaw, K. S., Tolbert, M. A., Lait, L. R., Dhaniyala, S., Flagan, R. C., Wennberg, P. O., Mahoney, M. J., Herman, R. L., Toon, G. C., and Bui, T. P.: An analysis of large HNO3-containing particles sampled in the Arctic stratosphere during the winter of 1999/2000, J. Geophys. Res. Atmos., 107, 8298, doi:10.1029/2001JD001079, 2002.

Peter, T.: Microphysics and heterogeneous chemistry of polar stratospheric clouds, Annu. Rev. Phys. Chem., 48, 785-822, doi:10.1146/annurev.physchem.48.1.785, 1997.

Pitts, M. C., Poole, L. R., and Thomason, L. W.: CALIPSO polar stratospheric cloud observations: second-generation detection algorithm and composition discrimination, Atmos. Chem. Phys., 9, 7577-7589, https://doi.org/10.5194/acp-9-7577-2009, 2009.

Pitts, M. C., Poole, L. R., Dörnbrack, A., and Thomason, L. W.: The 2009–2010 Arctic polar stratospheric cloud season: a CALIPSO perspective, Atmos. Chem. Phys., 11, 2161-2177, https://doi.org/10.5194/acp-11-2161-2011, 2011.

Pitts, M. C., Poole, L. R., Lambert, A., and Thomason, L. W.: An assessment of CALIOP polar stratospheric cloud composition classification, Atmos. Chem. Phys., 13, 2975-2988, https://doi.org/10.5194/acp-13-2975-2013, 2013.

Poole, L. R., and M. C. Pitts, pers. comm.: The CALIPSO Version 2 Polar Stratospheric Cloud Detection and Composition Classification Algorithm, to be submitted to Atmos. Meas. Tech. Disc., 2017.

5 Popp, P. J. , T. Marcy, L. A. Watts, R. Gao, D. W. Fahey; E. Weinstock, J. Smith, B. Herman, R. F. Troy, C. Webster, L. Christensen, D. Baumgardner, C. Voigt, B. Kärcher, C. Wilson, M. Mahoney, E. Jensen, P. Bui, Condensed-phase nitric acid in a tropical subvisible cirrus cloud, Geophys. Res. Lett., 34, L24812, doi:10.1029/ 2007GL031832, 2007.

Powell, K. A., C. A. Hostetler, M. A. Vaughan, K. Lee, C. R. Trepte, R. R. Rogers, D. M. Winker, Z. Liu, R. E. Kuehn, W. H. Hunt, and S. A. Young: CALIPSO Lidar Calibration Algorithms. Part I: Nighttime 532-nm Parallel Channel and 532-nm

10 Perpendicular Channel, J. Atmos. Oceanic Technol., 26, 2015–2033, https://doi.org/10.1175/2009JTECHA1242.1, 2009.

Schiller, C., R. Bauer, F. Cairo, T. Deshler, A. Dörnbrack, J. Elkins, A. Engel, H. Flentje, N. Larsen, I. Levin, M. Müller, S. Oltmans, H. Ovarlez, J. Ovarlez, J. Schreiner, F. Stroh, C. Voigt, H. Vömel, Dehydration in the Arctic stratosphere during the SOLVE/THESEO-2000 campaigns, J Geophys Res-Atmos, 107 (D20), 8293, doi:10.1029/2001JD000463, 2002.

Schreiner, J., Voigt, C., Kohlmann, A., Arnold, F., Mauersberger, K., and Larsen, N.: Chemical Analysis of Polar

15 Stratospheric Cloud Particles, Science, 283, 968–970, doi:10.1126/science.283.5404.968, 1999.

Schreiner J., U. Schild, C. Voigt, K. Mauersberger, Focussing of aerosols into a particle beam at pressures from 10 to 150 torr, Aerosol Sci. Technol., 31, 373-382, doi:10.1080/02786829808965550, 1999.

 Schreiner, J., C. Voigt, C. Weisser, A. Kohlmann, K. Mauersberger, T. Deshler, C. Kröger, J. Rosen, N. Kjome, N. Larsen, A. Adriani, F. Cairo, G. Di Donfrancesco, J. Ovarlez, H. Ovarlez, and A. Dörnbrack: Chemical, microphysical, and optical

20 properties of polar stratospheric clouds, J Geophys Res-Atmos, 107, 8313, doi:10.1029/2001JD00082, 2002.

Sinnhuber, B. M., Stiller, G., Ruhnke, R., von Clarmann, T., Kellmann, S., and Aschmann, J.: Arctic winter 2010/2011 at the brink of an ozone hole, Geophys Res Lett, 38, doi:10.1029/2011gl049784, 2011.

Solomon, S., Garcia, R. R., Rowland, F. S., and Wuebbles, D. J.: On the Depletion of Antarctic Ozone, Nature, 321, 755-758, doi:10.1038/321755a0, 1986.

25 Solomon, S.: The hole truth - What's news (and what's not) about the ozone hole., Nature, 427, 289-291, doi:10.1038/427289a, 2004.

Toon, O. B., Turco, R. P., Jordan, J., Goodman, J., and Ferry, G.: Physical Processes in Polar Stratospheric Ice Clouds, J Geophys Res-Atmos, 94, 11359-11380, doi:10.1029/Jd094id09p11359, 1989.

Toon, O. B., Tabazadeh, A., Browell, E. V., and Jordan, J.: Analysis of lidar observations of Arctic polar stratospheric

30 clouds during January 1989, J Geophys Res-Atmos, 105, 20589-20615, doi:10.1029/2000jd900144, 2000.

Voigt, C., Schreiner, J., Kohlmann, A., Zink, P., Mauersberger, K., Larsen, N., Deshler, T., Kroger, C., Rosen, J., Adriani, A., Cairo, F., Di Donfrancesco, G., Viterbini, M., Ovarlez, J., Ovarlez, H., David, C., and Dörnbrack, A.: Nitric Acid Trihydrate (NAT) in Polar Stratospheric Clouds, Science, 290, 1756–1758, doi:10.1126/science.290.5497.1756, 2000.

Voigt, C., S. Tsias, A. Dörnbrack, S. Meilinger, B.P. Luo, J. Schreiner, N. Larsen, K. Mauersberger, T. Peter, Non-equilibrium compositions of liquid polar stratospheric clouds in gravity waves, Geophys. Res. Lett, 27(23), 3873-3876, doi:10.1029/2000GL012168, 2000.

Voigt, C., Larsen, N., Deshler, T., Kroger, C., Schreiner, J., Mauersberger, K., Luo, B. P., Adriani, A., Cairo, F., Di Donfrancesco, G., Ovarlez, J., Ovarlez, H., Dornbrack, A., Knudsen, B., and Rosen, J.: In situ mountain-wave polar stratospheric cloud measurements: Implications for nitric acid trihydrate formation, J Geophys Res-Atmos, 108, doi:10.1029/2001jd001185, 2003.

Voigt, C., Schlager, H., Luo, B. P., Dörnbrack, A., Roiger, A., Stock, P., Curtius, J., Vössing, H., Borrmann, S., Davies, S., Konopka, P., Schiller, C., Shur, G., and Peter, T.: Nitric Acid Trihydrate (NAT) formation at low NAT supersaturation in Polar Stratospheric Clouds (PSCs), Atmos. Chem. Phys., 5, 1371-1380, doi:10.5194/acp-5-1371-2005, 2005.

Voigt, C., H. Schlager, A. Roiger, A. Stenke, M. de Reus, S. Borrmann, E. Jensen, C. Schiller, P. Konopka, N. Stinikov, Detection of NOy containing particles in the tropopause region - evidence for a tropical nitric acid trihydrate (NAT) belt, Atmos. Chem. Phys., 8, 7421-7430, doi:10.5194/acp-8-7421-2008, 2008.

Voigt, C., Dörnbrack, A., Wirth, M., Groß, S. M., Baumann, R., Ehard, B., Pitts, M. C., Poole, L. R., Sinnhuber, B.-M., and Oelhaf, H.: Widespread persistent polar stratospheric ice clouds in the Arctic, Atmos. Chem. Phys. Discuss., https://doi.org/10.5194/acp-2016-1082, 2016.

von Hobe, M., Bekki, S., Borrmann, S., Cairo, F., D'Amato, F., Di Donfrancesco, G., Dornbrack, A., Ebersoldt, A., Ebert, M., Emde, C., Engel, I., Ern, M., Frey, W., Genco, S., Griessbach, S., Grooss, J. U., Gulde, T., Gunther, G., Hosen, E., Hoffmann, L., Homonnai, V., Hoyle, C. R., Isaksen, I. S. A., Jackson, D. R., Janosi, I. M., Jones, R. L., Kandler, K., Kalicinsky, C., Keil, A., Khaykin, S. M., Khosrawi, F., Kivi, R., Kuttippurath, J., Laube, J. C., Lefevre, F., Lehmann, R., Ludmann, S., Luo, B. P., Marchand, M., Meyer, J., Mitev, V., Molleker, S., Muller, R., Oelhaf, H., Olschewski, F., Orsolini, Y., Peter, T., Pfeilsticker, K., Piesch, C., Pitts, M. C., Poole, L. R., Pope, F. D., Ravegnani, F., Rex, M., Riese, M., Rockmann, T., Rognerud, B., Roiger, A., Rolf, C., Santee, M. L., Scheibe, M., Schiller, C., Schlager, H., de Cumis, M. S., Sitnikov, N., Sovde, O. A., Spang, R., Spelten, N., Stordal, F., Suminska-Ebersoldt, O., Ulanovski, A., Ungermann, J., Viciani, S., Volk, C. M., Scheidt, M. V., von der Gathen, P., Walker, K., Wegner, T., Weigel, R., Weinbruch, S., Wetzel, G., Wienhold, F. G., Wohltmann, I., Woiwode, W., Young, I. A. K., Yushkov, V., Zobrist, B., and Stroh, F.: Reconciliation of essential process parameters for an enhanced predictability of Arctic stratospheric ozone loss and its climate interactions (RECONCILE): activities and results, Atmos. Chem. Phys., 13, 9233-9268, 10.5194/acp-13-9233-2013, 2013.

Weiss, F., Kubel, F., Galvez, O., Hoelzel, M., Parker, S. F., Baloh, P., Iannarelli, R., Rossi, M. J., and Grothe, H.: Metastable Nitric Acid Trihydrate in Ice Clouds, Angew. Chem. Int. Edit., 55, 3276, doi:10.1002/anie.201510841, 2016.

Weigel, R., Volk, C. M., Kandler, K., Hösen, E., Günther, G., Vogel, B., Grooß, J.-U., Khaykin, S., Belyaev, G. V., and Borrmann, S.: Enhancements of the refractory submicron aerosol fraction in the Arctic polar vortex: feature or exception?, Atmos. Chem. Phys., 14, 12319-12342, doi:10.5194/acp-14-12319-2014, 2014.

Wirth, M., Fix, A., Mahnke, P., Schwarzer, H., Schrandt, F., and Ehret, G.: The airborne muli-wavelength water vapor differential absorption lidar WALES: system design and performance, Appl. Phys. B, 96, 201 - 213, doi:0.1007/s00340-009-3365-7, 2009.

Wohltmann, I., Wegner, T., Muller, R., Lehmann, R., Rex, M., Manney, G. L., Santee, M. L., Bernath, P., Suminska-Ebersoldt, O., Stroh, F., von Hobe, M., Volk, C. M., Hosen, E., Ravegnani, F., Ulanovsky, A., and Yushkov, V.: Uncertainties in modelling heterogeneous chemistry and Arctic ozone depletion in the winter 2009/2010, Atmos. Chem. Phys., 13, 3909-3929, doi:10.5194/acp-13-3909-2013, 2013.

Woiwode, W., Grooss, J. U., Oelhaf, H., Molleker, S., Borrmann, S., Ebersoldt, A., Frey, W., Gulde, T., Khaykin, S., Maucher, G., Piesch, C., and Orphal, J.: Denitrification by large NAT particles: the impact of reduced settling velocities and hints on particle characteristics, Atmos. Chem. Phys., 14, 11525-11544, doi:10.5194/acp-14-11525-2014, 2014.

Woiwode, W., Höpfner, M., Bi, L., Pitts, M. C., Poole, L. R., Oelhaf, H., Molleker, S., Borrmann, S., Klingebiel, M., Belyaev, G., Ebersoldt, A., Griessbach, S., Grooß, J.-U., Gulde, T., Krämer, M., Maucher, G., Piesch, C., Rolf, C., Sartorius, C., Spang, R., and Orphal, J.: Spectroscopic evidence of large aspherical β-NAT particles involved in denitrification in the December 2011 Arctic stratosphere, Atmos. Chem. Phys., 16, 9505-9532, https://doi.org/10.5194/acp-16-9505-2016, 2016.

Zondlo, M. A., Hudson, P. K., Prenni, A. J., and Tolbert, M. A.: Chemistry and microphysics of polar stratospheric clouds and cirrus clouds, Annu. Rev. Phys. Chem., 51, 473-499, doi:10.1146/annurev.physchem.51.1.473, 2000.
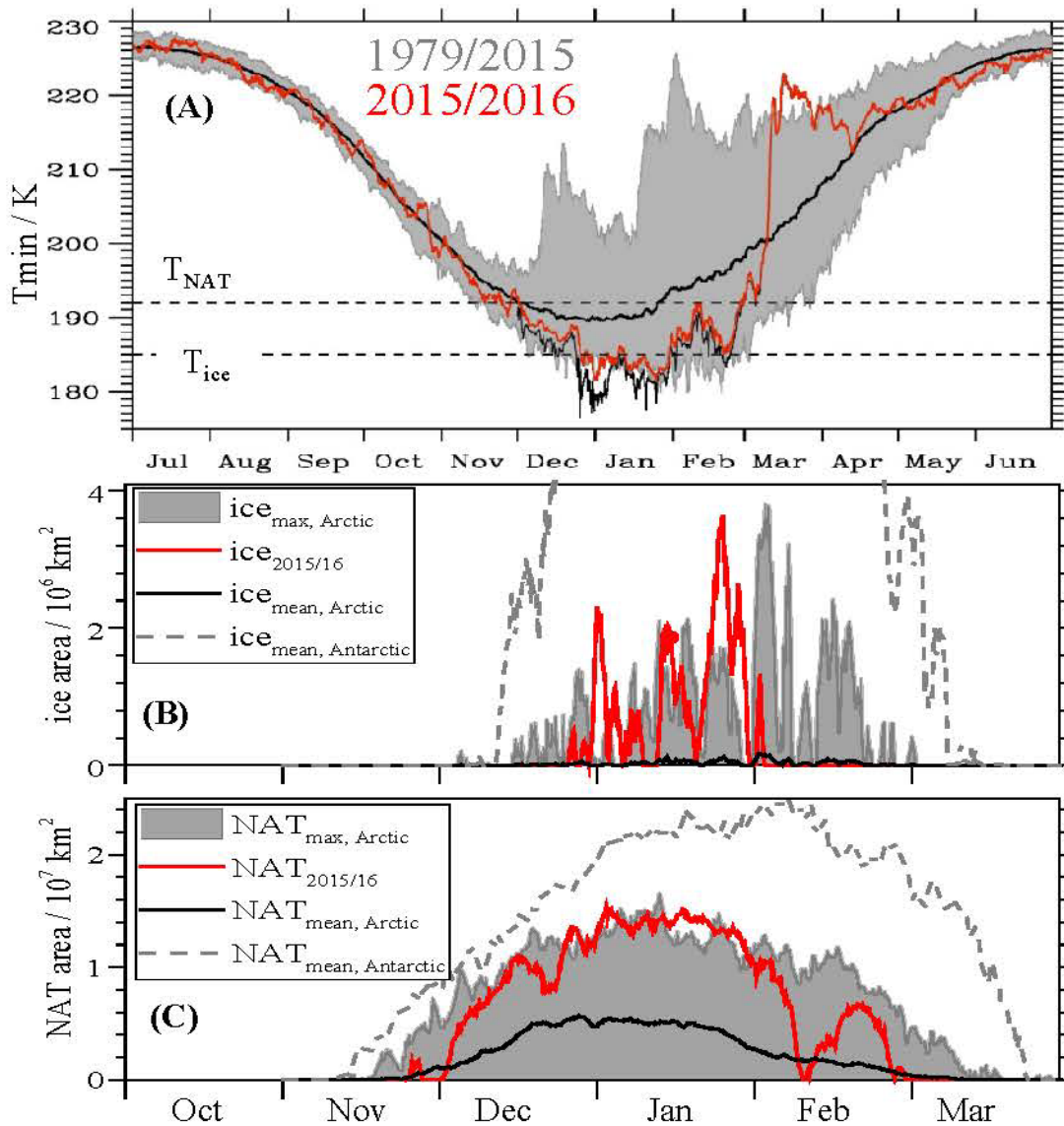
Figure 1: Temperature evolution of the 2015/2016 Arctic winter stratosphere (A) 6-hourly ECMWF ERA interim reanalysis (Dee et al. 2011) data retrieved at a horizontal resolution of 1°: minimum temperature T_{min} (K) between 65° and 90°N at the 30-hPa pressure surface. The thick black line denotes the mean values of T_{min} averaged during 1979 to 2015, and the shaded areas encompass the minimum and maximum values of T_{min} between 1979 and 2015. The red line marks the evolution of T_{min} from operational analyses of the IFS cycle 41r1 until 8 Mar 2016. The thin black line indicates T_{min} from the IFS cycle 41r2 in the preoperational phase from 1 December 2015 to 8 Mar 2016 retrieved at a resolution of 0.125°. After 8 March 2016, the black line continues as red curve of the operational IFS cycle 41r2. T_{ice} (Murphy and Koop, 2005) and T_{NAT} (Hanson and Mauersberger, 1988) are calculated using 4.6 ppmv H_2O and 7 ppbv HNO_3, relevant for the 2015/2016 Arctic vortex conditions (Manney and Lawrence, 2016). (B) Evolution of the vortex area with temperatures below T_{ice}. The black line marks the mean area below T_{ice} (A_{ice}) at 30 hPa pressure (~21.6 km) between 1979 and 2015. The gray shading indicates maximum and minimum A_{ice} in the same time period. The red line shows the evolution of A_{ice} at the 30 hPa pressure surface in the Arctic winter 2015/2016 of the IFS cycle 41r2. The gray dashed line gives the mean area below T_{ice} at 30 hPa south of 65°S from 1979 to 2015, shifted by 6 months to account for seasonality. (C) Same data for NAT.
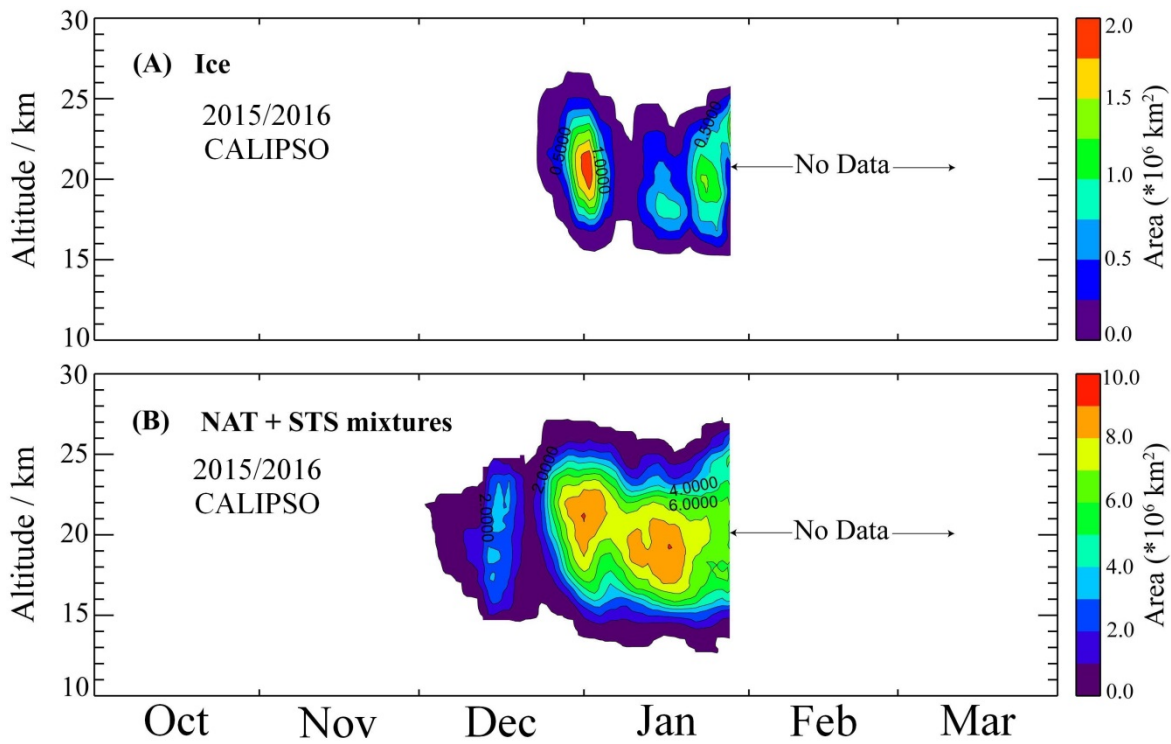
Figure 2: Curtain plot of the areal occurrence of PSCs in the winter 2015/2016 detected by the CALIOP lidar onboard the CALIPSO satellite using the classification from Pitts et al. (2013) modified as described in the text. (A) Curtain plot of ice PSC occurrence. (B) Curtain plot of NAT/STS PSC occurrence. Synoptic ice PSCs were observed by CALIOP from mid of December 2015 till end of January 2016.
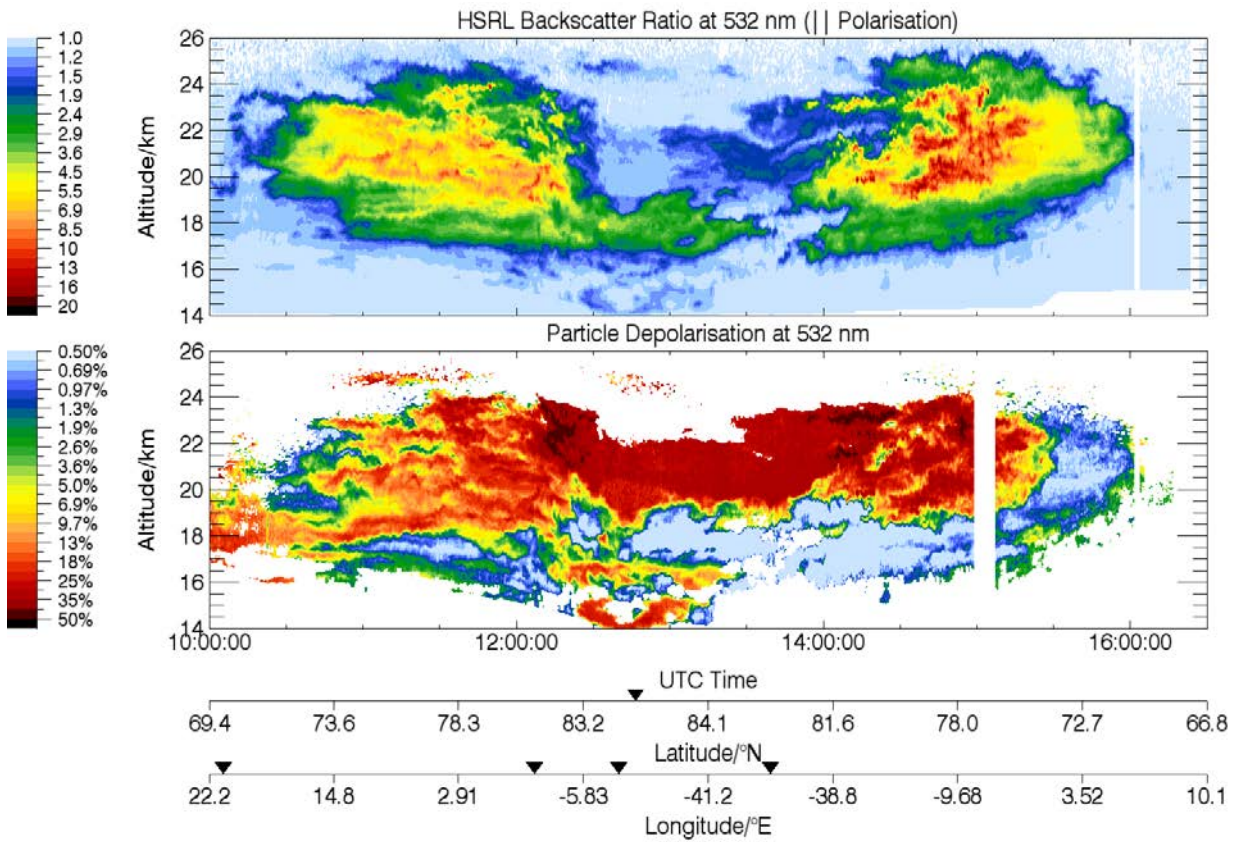
Figure 3 Lidar observation of a synoptic-scale polar stratospheric cloud observed on 22 January 2016 Upper panel: Backscatter ratios from the WALES lidar (Wirth et al., 2010) at 532 nm wavelengths during a HALO flight into the Arctic vortex. The particle depolarization is shown in the lower panel. The time of the flight, as well as latitude and longitude of the HALO flight path are indicated. Turning points of the HALO are marked by triangles.
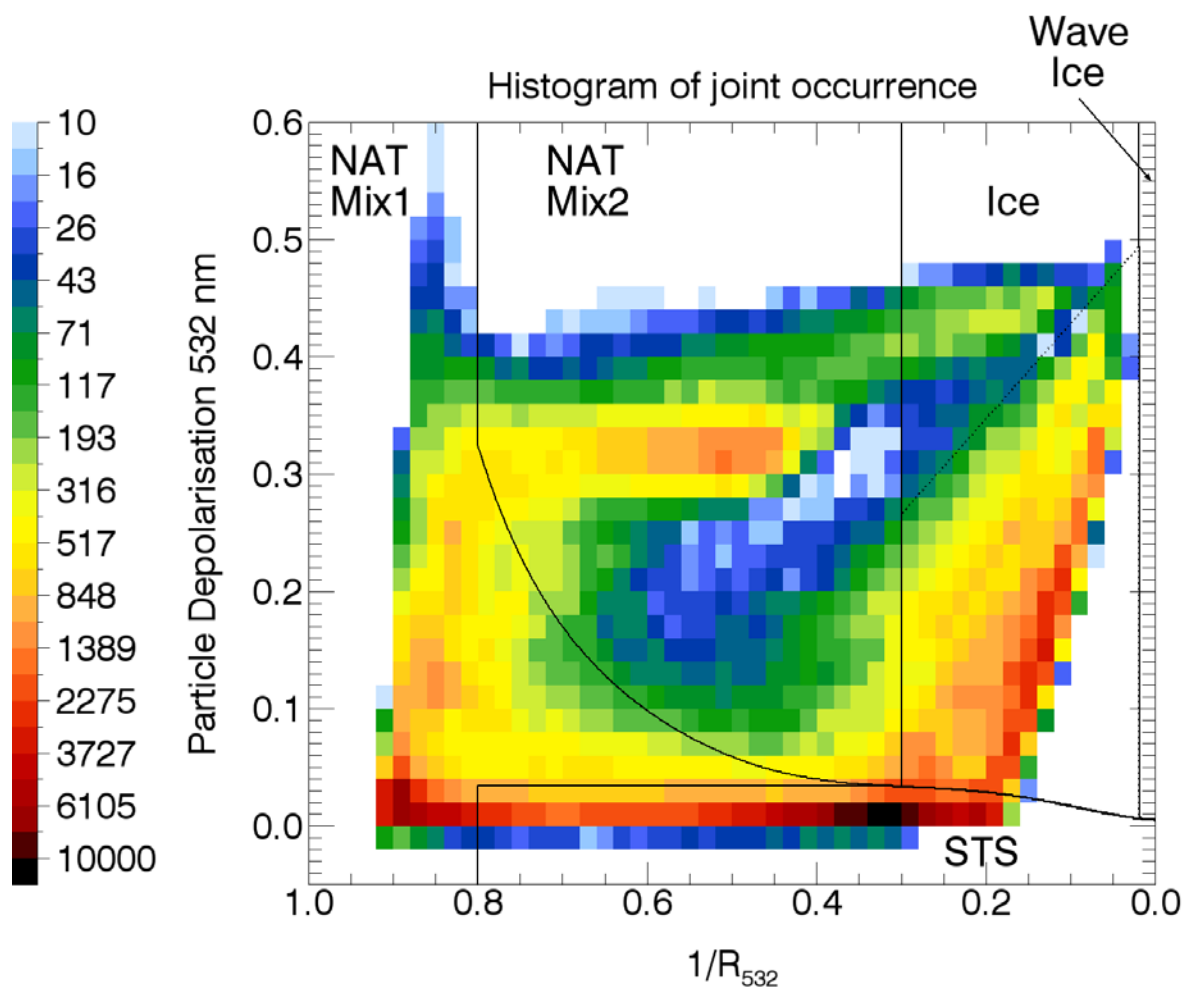
Figure 4 Composite 2-dimensional histogram of the PSC on 22 Janaury 2016 shown in Figure 3 in the 1/backscatter ratio versus aerosol-depolarization coordinate system. The solid black lines denote the boundaries of the PSC regimes defined by Pitts et al. (2011) with the threshold between ice and NAT/Mix2 $1/R_{ice|NAT} = 0.3$. A lower threshold $1/R_{ice|NAT} = 0.2$ would misclassify a fraction of the ice particles as NAT. The dotted line separates the upper and a lower ice branch.
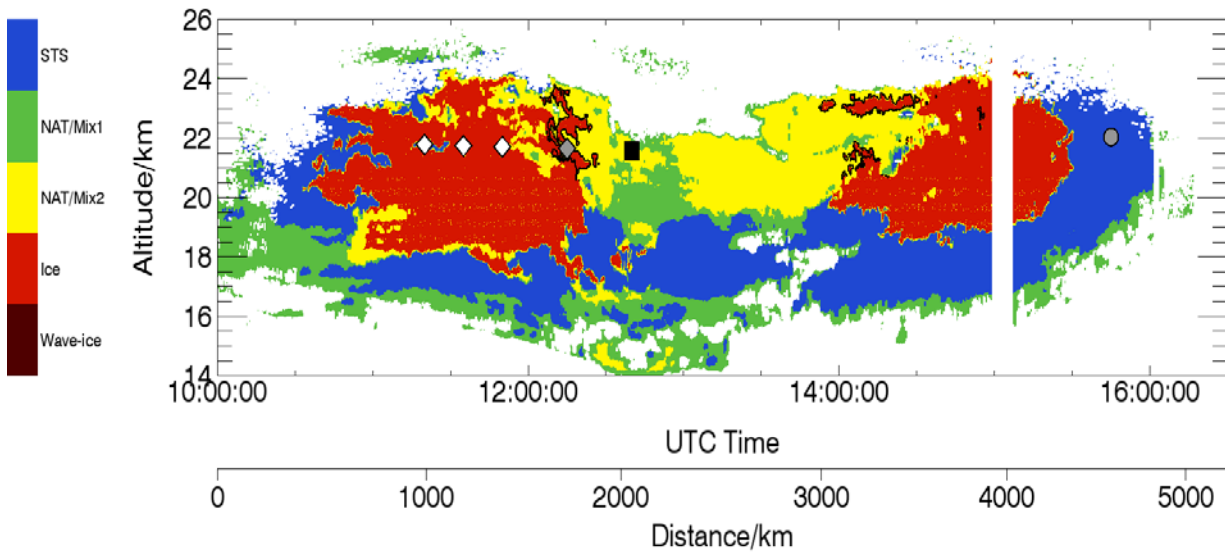
Figure 5 Classification of the synoptic-scale polar stratospheric ice cloud on 22 January 2016 shown in Figure 3. In addition to the classification after Pitts at al. (2011), we use $1/ R_{ice|NAT} = 0.3$ as threshold of ice versus NAT/Mix2 separation. A synoptic ice PSC (red area) extends over several hundred km above the HALO flight track. The ice PSC is embedded in NAT layers (NAT/Mix1, green; NAT/Mix2, yellow) and surrounded by liquid STS layers (blue). The wave-ice class is not populated. The ending points of the trajectories for ice (white and gray diamonds), NAT (black square) and STS (gray circle) given in Figure 7 are marked. The black line encloses the fraction of the ice PSC detected in the upper ice branch in Figure 4.
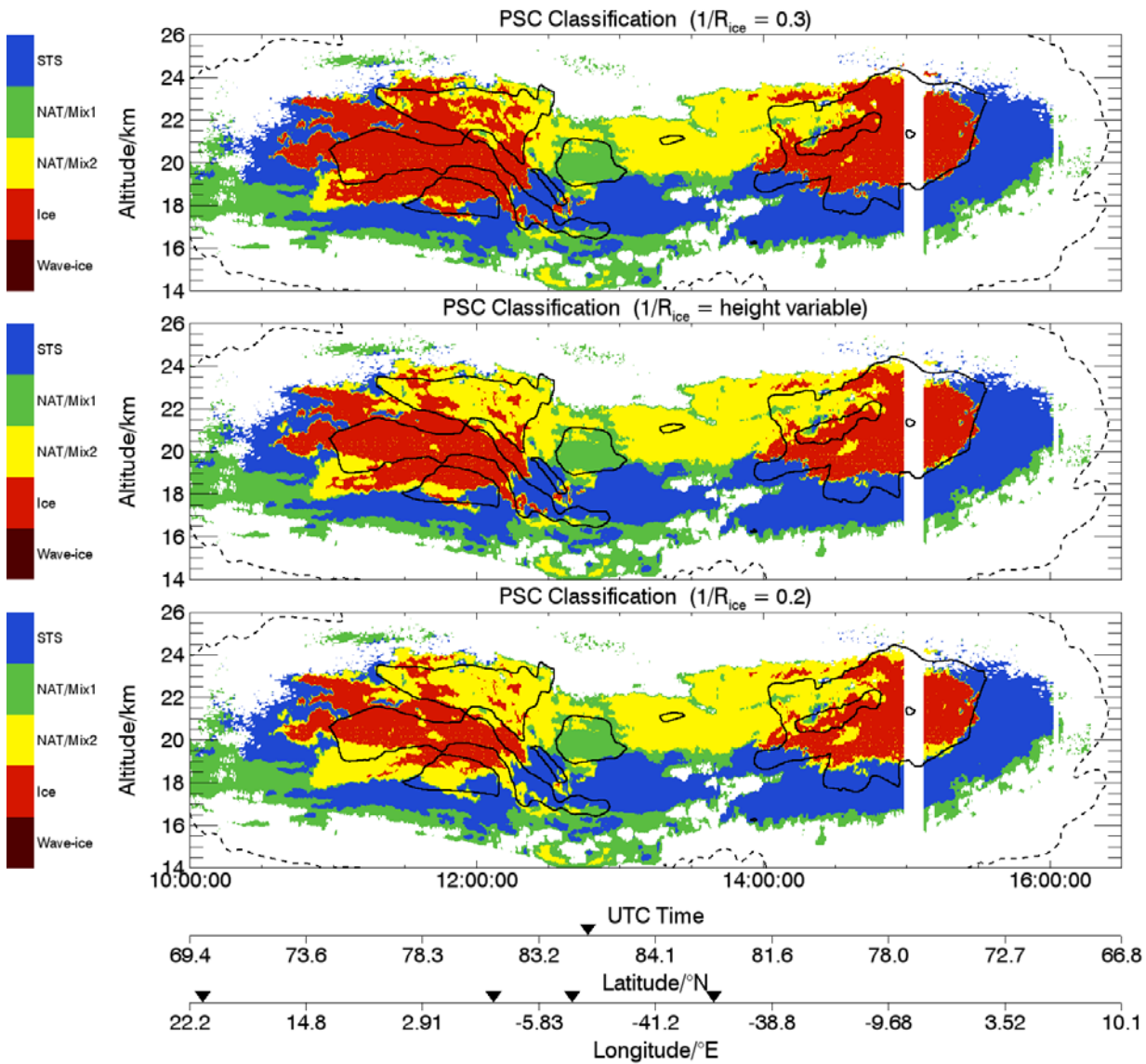
Figure 6 PSC type classifications for different thresholds $1/R_{ice|NAT}$ of ice versus NAT/Mix2 separation. The upper panel shows again the classification after Pitts et al. (2011), but with a boundary of $1/R_{ice|NAT} = 0.3$ as in Figure 5. The middle panel adopts an altitude dependent variation of the boundary between 0.2 and 0.3, based on MLS measurements of HNO_3 and H_2O. For the lower panel this threshold is set to $1/R_{ice|NAT} = 0.2$, the standard value of Pitts et al. (2009). In addition, the areas with temperatures below T_{NAT} (dashed line) and T_{ice} (solid line) as derived from 6-hourly IFS operational analysis (cycle 41r2) interpolated to 1-hourly time steps using forecast data, the water vapor field measured by WALES and a climatological HNO_3 profile are shown.
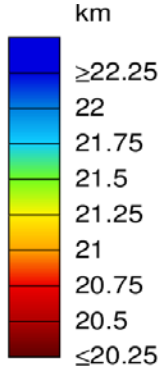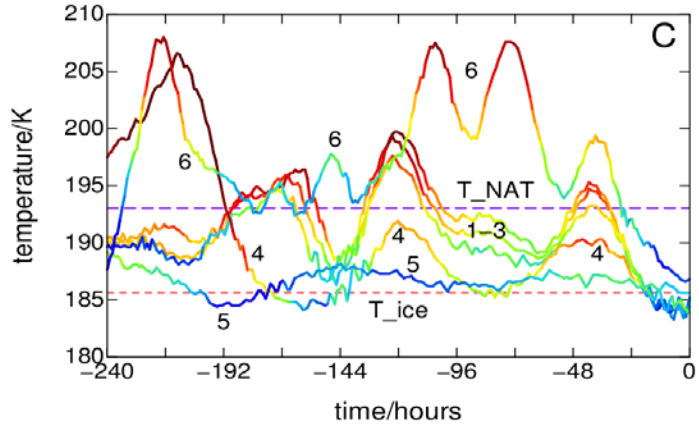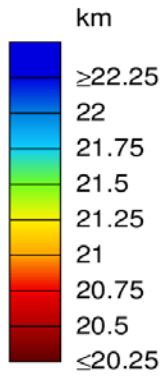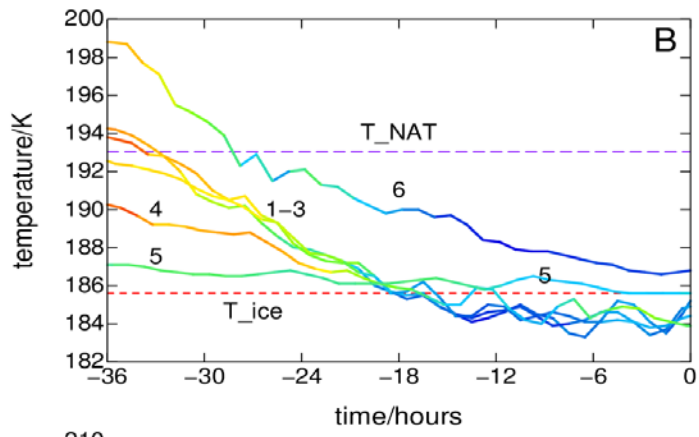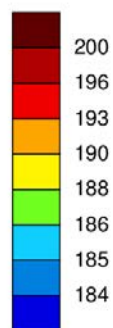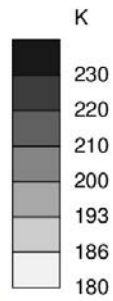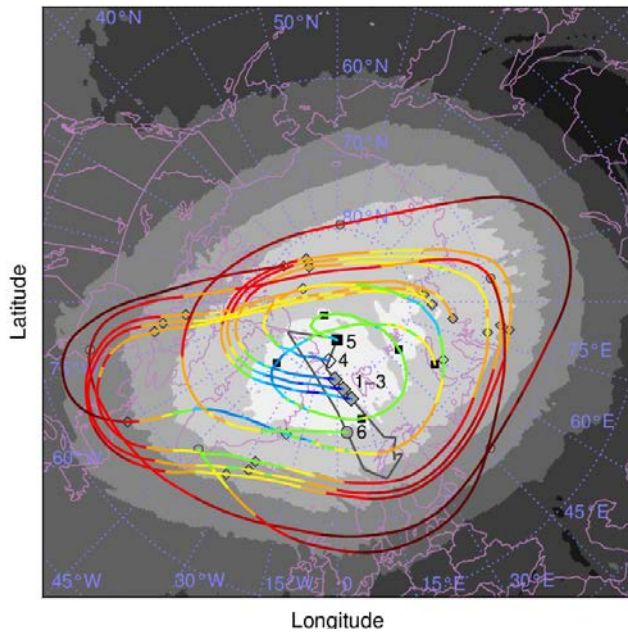
Figure 7 Temperature trajectories ending in the individual PSC layers measured on 22 January 2016 (A) Temperatures at 30 hPa (grey shading) on 22 January 2016 derived from the IFS operational analysis (cycle 41r1). The HALO flight track is shown as gray line. The path of six representative 10-days back-trajectories starting at 30 hPa pressure level are color coded by temperature. Their starting points in the ice PSC (diamonds, numbered chronologically along the flight path 1 - 4), in the NAT layer (black square, 5) and in the STS layer (gray circle, 6) are indicated, see also Figure 5. Time steps every 48 h are marked by the same, but smaller symbols on the back-trajectories. The temperature evolution along these trajectories is shown in panel (B) and (C), with panel (B) focusing on the last 36-h for enhanced readability. Color coding represents the altitude along the trajectories. T_{ice} and T_{NAT}, depicted by dashed lines, are calculated from Murphy and Koop (2005) and Hanson and Mauersberger (1988) for 4.6 ppmv H_2O and 7 ppbv HNO_3, respectively.